Low-Cost, Multifunctional, and Sustainable Sodium Sulfido Ferrate(II)

Mohammad R. Ghazanfari, Konrad Siemensmeyer, Archa Santhosh, Johannes C. Vrijmoed, Mirko Tallu, Stefanie Dehnen, Paul Jerabek, and Günther Thiele*

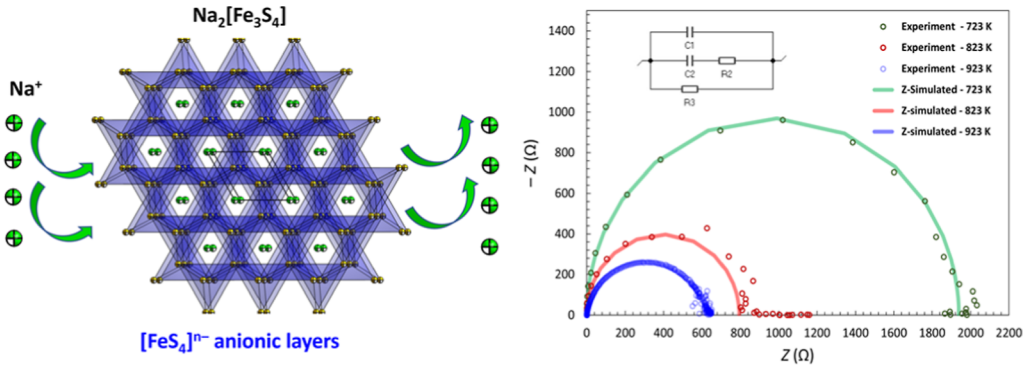

ABSTRACT: We introduce $Na_2[Fe_3S_4]$, comprising anionic layers, synthesized by a simple and straightforward solid-state method based on the fusion of binary sulfides of abundant sodium and iron. The structure crystallizes in a trigonal lattice with honeycomb cavities, as well as 25% of statistical iron vacancies in the crystal structure. The compound depicts high dielectric constants from 998 to 1850 at a frequency of 1 kHz depending on the sintering temperature, comparable with benchmark dielectric materials. According to the complex electrochemical impedance results, the compound depicts an electrical conductivity at ambient temperature. Optical investigations reveal a band gap of 1.64 eV, which is in agreement with an electronic band gap of 1.63 eV computed by density functional theory calculations. Magnetometry results reveal an antiferromagnetic behavior with a transition at 120 K. These findings introduce $Na_2[Fe_3S_4]$ as a sustainable multifunctional material with potential for a variety of electronic and magnetic applications.

1. INTRODUCTION

Nowadays, electronic devices based on new technologies—from smartphones to electrical vehicles—are an integral part of the everyday life. Solid-state inorganic materials are at the heart of these devices to facilitate different applications, such as semiconductors, capacitors, superconductors, electromagnetic sensors, and solid-state batteries.[1−3] Although solid-state electronic materials are known for an inherent energy efficiency, reliability, longevity, and durability, their sustainability is still a controversial issue. In most of the current electronic and magnetic devices, the essential materials contain toxic constituents and/or are based on limited resources. In particular, the raw material supply processes of current commercial energy-storage technologies are questioned for their dramatic impacts on the environment and social communities.[4−6] As an example, lithium-ion batteries are the flagship members of energy storage technologies and are widely utilized in electronic devices.[4] However, the drawbacks include high costs,[2] limited resources,[5] and the environmental and social challenges of lithium mining.[6] To overcome these challenges, new materials for different types of battery cells, such as sodium- and potassium-ion batteries,[7] iron−sulfur batteries,[8] and zinc−air batteries,[9] are continuously designed and introduced for the new generation of electrical energy storage devices. Among them, sodium-ion batteries are promising candidates due to their reasonable power density, abundant sodium resources, and sustainability.[10] While some of the electrochemical properties of commercial energy storage devices seem auspicious, the abundancy of the redox−active transition metals displays a serious concern. In particular, the elements cobalt, nickel, and vanadium are prominently found in battery materials, all of which are critical resources. In contrast, sodium, iron, and sulfur are highly abundant and nontoxic and can be sourced from environmentally and socially controlled mining processes.

We have recently reported on the high dielectric constant and the second highest bulk ionic conductivity of K-ion containing materials in $K_2[Fe_3S_4]$, a ternary sulfido ferrate containing iron vacancies in the anionic substructure.[11] We were, therefore, interested in the sodium analogue, $Na_2[Fe_3S_4]$ (**1**), which should combine high dielectric constants and high ionic conductivity values with abundant and nontoxic elemental components. Owing to the abundant sources of sodium compared to those of potassium, as well as further potentials and an increasing interest in sodium-ion batteries, **1** is a promising candidate to synthesize and investigate in comparison with the potassium analogue. We here present a comprehensive study on the successful isolation of **1**, including large-scale and single-crystal syntheses, dielectric and impedance analyses, as well of further investigations including magnetic, thermal, and optical properties alongside first-principles calculations.

2. EXPERIMENTAL SECTION

2.1. Materials and General Procedure. Sodium (Onyxmet, 99.8%), sulfur (abcr, 99% sublimed), and iron sulfide (FeS, Sigma-Aldrich) were commercially purchased and used without any further purification. Na_2S is synthesized under an argon atmosphere according to the reported protocol[12] by dissolving 21.65 g (0.94 mol, 2 equiv) of sodium in approx. 250 mL of liquid ammonia at a temperature of 200 K, then gradually adding 15.07 g (0.47 mol, 1 equiv) of sulfur at a temperature of 240 K, and stirring the mixture for approx. 12 h while allowing it to very slowly heat up to room temperature. During this time, the ammonia will evaporate, thus facilitating the release of pressure. The purity of as-synthesized Na_2S was verified by the powder X-ray diffraction (P-XRD). Special attention should be directed throughout the synthesis to provide a pressure release option while working with liquefied gases as solvents. The addition of sulfur must not be performed at temperatures below 240 K due to potential kinetic hindrance of the reaction at lower temperatures, which may result in a thermal runaway reaction upon later heating.

Due to the air and moisture sensitivity of Na_2S and **1**, all manipulations including the synthesis, handling, and characterization procedures were carried out under an inert atmosphere in argon-filled gloveboxes or using standard Schlenk techniques.

2.2. Synthetic Procedure of 1. 7.80 g (0.1 mol, 1 equiv) of Na_2S and 16.74 g (0.3 mol, 3 equiv) of FeS were mixed uniformly and placed into a silica glass ampule. The ampule was heated to approx. 1100 K for around 6 min using a methane-oxygen flame torch and subsequently allowed to cool to room temperature. The crude product was manually removed and ground. 21.24 g (86% yield) of **1** was obtained as a dark green powder. While removing the reaction product from the ampoule, the adhered material at the glass surface was disposed to prevent contamination with glass pieces and/or potential undesired phases, possibly obtained from side reaction with the glass surface. This reduced the overall yield. To prepare single crystals of **1**, a solvothermal treatment was conducted at 423 K for 48 h by placing 125 mg of as-synthesized powder of **1** in a 10 mL vial with 2 mL of pyridine as a solvent.

2.3. Structural, Microstructural, and Thermal Analyses. *2.3.1. PXRD and Rietveld Structure Refinement.* To conduct PXRD measurements, the sample was prepared by placing approx. 10 mg of fine powder of **1** in between two layers of Scotch tape (ScotchMagic dull-transparent) to prevent any exposure to air or moisture. The measurement was carried out using a STOE MP diffractometer equipped with a Dectris Mythen 1K linear silicon strip detector and a Ge(111) double-crystal monochromator operating at 40 kV and 50 mA in transmission configuration using Mo K_α radiation (λ = 0.71073 Å) at 293 K in the 2θ range of 5 to 45°. The purity, degree of crystallinity, and average crystallite size of **1** were determined by Rietveld structure refinement[13] using GSAS II[14] software.

2.3.2. Single-Crystal X-ray Diffraction. A suitable crystal from the solvothermal treatment is isolated under an optical microscope, mounted in Paratone oil, and stored in a liquid nitrogen container according to the reported protocol.[15] Measurements were performed using a Bruker D8 Venture diffractometer with Mo K_α radiation (λ = 0.71073 Å) at 100 K. The crystal structure was solved and refined using Olex2[16] software with ShelXT[17] and ShelXL[18] programs, respectively, and then depicted with the DIAMOND4.5.2 software package.[19] Refinement details as well as solved crystal structure data are provided in the Supporting Information file.

2.3.3. Energy-Dispersive X-ray Spectroscopy. Approx. 10 mg of fine powder of **1** was deposited on a measurement stub using a carbon sticker and subsequently carbon-coated to prevent charge accumulation on the surface and then transferred to a scanning electron microscope [Zeiss Sigma 300VP field-emission-scanning electron microscope (FE-SEM)] coupled with EDX (Bruker, Quantax Xflash 6, 60 mm^2 SSD EDS) detectors. Measurements were done at a working distance of 8.5 mm, a beam aperture of 60 mm, and a beam energy of 20 kV. The Bruker Esprit 2.1 software was used for postprocess quantitative analysis of the EDX measurements.

2.3.4. Thermal Analyses. To investigate the thermal properties of the compound, thermal analyses including thermal gravimetry (TG) coupled with differential scanning calorimetry (DSC) measurements were carried out under an inert atmosphere in the range of room temperature to a temperature of 1200 K for two successive heating−cooling cycles. More details on the samples preparation and the measurements are available in the Supporting Information.

2.4. Dielectric and Impedance Measurements. *2.4.1. Preparation of Pellets and Sintering.* To measure the electrical parameters, the samples were prepared as pellets by pressing and sintering. Approx. 400 mg of fine powder (average particle size < 2 μm) of **1** was placed into a cylindrical pressing mold, sealed with a parafilm, and pressed using a uniaxial hydraulic press (Paul Weber Maschinen, 200 kN) up to 80 kN·cm^{-2}. Afterward, the pellets were transferred into a silica glass ampule, sintered at temperatures of 723, 823, or 923 K for 12 h, and labeled as **1**-723, **1**-823, and **1**-923, respectively. The possible sintering temperatures were limited by the melting point of around 950 K (see Supporting Information). The pellet dimensions before sintering were 13 mm in diameter and 2 mm in thickness and then shrunk during sintering to 11.8 (11.7, 11.2) mm in diameter and 1.6 (1.6, 1.5) mm in thickness for **1**-723 (**1**-823, **1**-923). To prepare the samples for electrical measurements, electrode layers were attached to both sides of the pellets by adding silver conductive adhesive paste (abcr, resistivity < 3.8×10^{-3} Ω cm^{-1}), conjugating standard conductive wires (copper/chromel-A, 0.22 mm/0.28 mm, PU 200 g), and heating at 420 K for 60 min in an electrical furnace. The microstructural properties of the sintered samples were investigated by imaging on the cross-section of pellets using a Zeiss Sigma 300VP field emission scanning electron microscope and the secondary electron detector.

2.4.2. Dielectric Measurements. Electrical parameters of the pellets including capacitance, resistance, reactance, and dielectric loss were measured at ambient temperature using an LCR meter (East Tester, ET4410) in the frequency range of 0.1 to 100 kHz with an applying voltage of 1 V and an external resistivity of 100 Ω.

2.4.3. Impedance Measurements. Complex impedance parameters of pellets were measured at 293 K using an electrochemical impedance analyzer (BioLogic MTZ-35). Measurements were done in a frequency range of 100 mHz to 1 MHz under 100 mV sine phase and a resolution voltage of 50 μV. The electrical conductivity of the samples was calculated using the complex impedance plots based on the Nyquist equation.[20] The simulation of complex impedance for the equivalent circuit was calculated using the ZSimpWin program.[21]

2.5. Magnetometry. Approx. 20 mg of fine powder of **1** was manually pressed into polyethylene microcapsules, inserted into a superconducting quantum interference device magnetometer (SQUID, MPMS3-7T Quantum Design), and measured in the temperature range of 3 to 370 K under a helium atmosphere. The field-dependent magnetization measurements were performed at five different temperatures of 3, 50, 100, 200, and 300 K by applying an

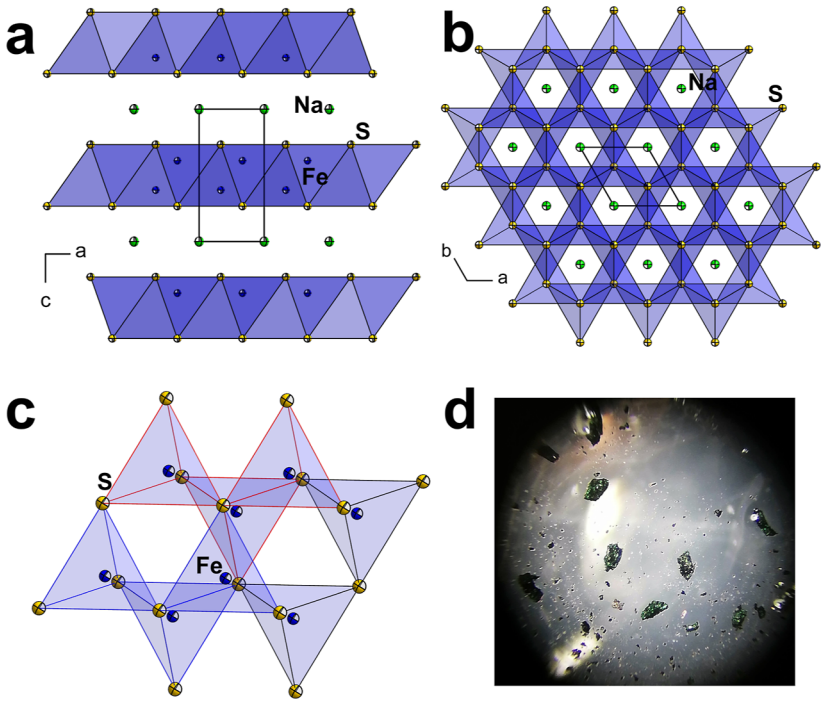

Figure 1. Representation of the crystal structure of **1** (a) along the crystallographic *b*-axis including edge-sharing $[FeS_4]^{6-}$-tetrahedra forming a 2D anionic sublattice perpendicular to the crystallographic *c*-axis; (b) along the crystallographic *c*-axis, displaying honeycomb-like cavities within the anionic layers; (c) depicting two corner-sharing tetrahedra sublattices with blue and red edges, respectively, forming the honeycomb-like cavities; both are crystallographically identical. (d) Optical microscopy photograph of single crystals of **1** at 80× magnification. Selected bond lengths and angles: Fe−S: 2.3213(8)−2.3697(3) Å, Na−S: 2.8654(4) Å, and S−Fe−S: 108.628(1)-110.302(3)°. Partial occupations of iron atoms are omitted for clarity.

external field up to 5.00 T. Zero-field cooling (ZFC) and field cooling (FC) investigations were carried out at a constant magnetic field of 50 mT. The obtained results were normalized according to the weight of the samples.

2.6. UV−Visible Spectroscopy. Approx. 5 mg of fine powder of **1** was inserted into a Praying Mantis accessory, and measurements were conducted by recording the optical reflection spectra using a Varian Cary 5000 UV/VIS/NIR spectrometer in the wavelength range of 200 to 1400 nm. Tauc plots were plotted for the measured diffuse reflectance, and the optical band gap was estimated by applying the Kubelka−Munk function.[22] More details are provided in the Supporting Information.

2.7. Quantum Chemical Calculations. Vienna ab initio simulation package version 5.4.4 (VASP)[23] was used for performing the spin-polarized density functional theory (DFT) calculations of **1** including the electronic band structure as well as density of states (DOS) based on generalized gradient approximation (GGA)[24] with the Perdew−Burke−Ernzerhof (PBE) exchange correlation functional.[25] The band structure is visualized along the high-symmetry paths in the Brillouin zone, and the energies of the computed bands are normalized to set the Fermi level to zero to ease viewing. More details of the calculations are provided in the Supporting Information.

3. RESULTS AND DISCUSSION

3.1. Synthesis and Structural Properties. **1** is synthesized through a straightforward and comparably fast (heat treatment for 6 min) solid-state reaction of an intimate mixture of 1 equiv of Na_2S and 3 equiv of FeS according to eq 1.

$$Na_2S + 3FeS \xrightarrow[\approx 6\ \text{min}]{\approx 1100\ \text{K}} Na_2[Fe_3S_4] \quad (1)$$

The reaction yielded around 86% of pure powder of **1** of dark green color. The reaction is scalable and only limited by the volume of the reaction container. **1** crystallizes in the $P\bar{3}m1$ space group with two chemical formula moieties per unit cell with a = 3.8495 (3) Å, c = 6.7606 (5) Å, V = 86.761 (15) Å^3. The crystal structure is a defect-variant of the $CaAl_2Si_2$ structure type[26] and consists of layered sublattices of anionic $[Fe_3S_4]$ with sodium ions in between these layers. In the anionic sublattice, the iron ions are tetrahedrally coordinated by sulfur atoms, and the resulted $[Fe^{II}S_4]^{6-}$ tetrahedra are edge-sharing (Figure 1). Within the anionic layers, there are structural honeycomb-shape cavities that are surrounded by three adjacent $[FeS_4]$-tetrahedra (Figure 1c). Iron atoms obtain 75% occupation according to the crystallographic refinement and EDX analysis, yielding "defects" within the anionic layers that are assumed to be statistically distributed due to the absence of superstructure reflexes or any other indications of ordering. To the best of our knowledge, there is only one isotypic sulfido ferrate salt reported, with a different occupation of the iron and sodium atoms, whereas electrical and impedance properties were not investigated.[26] We have recently reported a 2:3:4 stoichiometric ratio in $K_2[Fe_3S_4]$ with space group type $I4/mmm$. However, the only similarity of **1** with the potassium analogue is the layered anionic structure and the 75% occupation of iron atoms within the structure.[11] Despite the similarities in iron vacancies and cationic layers, these two compounds crystallize in two different lattice structures. In $K_2[Fe_3S_4]$, the edge-sharing tetrahedra create the anionic layers without any inherent structural voids, while in **1**, the edge- and corner-sharing tetrahedra induce honeycomb cavities in the anionic layers. The Fe−S bond lengths in **1** (2.3213(8)-2.3697(3) Å) are comparable to those obtained in $K_2[Fe_3S_4]$ (2.344(8) Å) as both coordination and formal oxidation state of iron atoms are identical. The smaller ionic

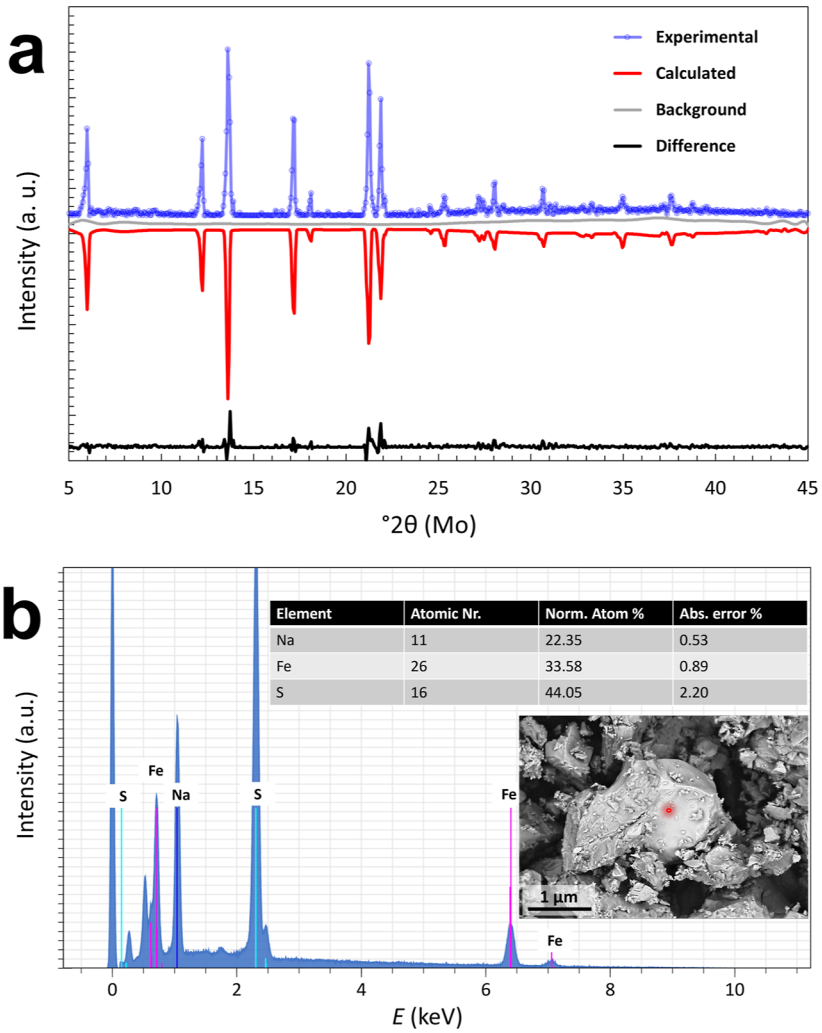

Figure 2. (a) Rietveld refinement results of as-synthesized **1**. (b) EDX spectrum of powder of **1**, with the extracted amounts of the elemental ratio, and a micrograph of the powder from backscattered electron signals at an applied beam energy of 20 kV using scanning electron microscopy.

radii of sodium ions compared to those of potassium ions lead to shorter distances between the anionic layers in **1** (3.64 Å) in comparison with $K_2[Fe_3S_4]$ (3.89 Å). To the best of our knowledge, **1** is a rare example of a ternary sodium sulfido ferrate in the formal oxidation state +II, alongside literature-known compounds of $Na_2[FeS_2]$[27] and $Na_6[FeS_4]$.[28]

The purity of **1** was confirmed by Rietveld structure refinement of the powder diffraction data (Figure 2a), and a crystallinity degree of 93% ± 3% and an average crystallite size of 248 nm ± 8 nm were obtained (for details, see Supporting Information). The elemental composition of **1** was confirmed by EDX measurements (Figure 2b), qualitatively indicating the purity and confirming the iron content according to a 75% occupation. Additional peaks for carbon (0.277 eV, K_α) and oxygen (0.523 eV, K_α) originate from the sample preparation and are discussed in the Supporting Information.

The thermal properties of the compound were evaluated by TG coupled with the DSC measurements. The results (Figure S1) indicate reversible endothermic and exothermic events at around 950 K during heating and cooling cycles, respectively, which are attributed to the melting point of **1**. In addition, the weight losses of 9.4% at temperatures higher than 1050 K in the first heating cycle and 4.7% at temperatures higher than 1100 K in the second heating cycle can be related to the (partial) decomposition of **1**. Further details on the thermal measurements are available in the Supporting Information.

3.2. Dielectric and Impedance Properties. The dielectric properties of **1** were investigated by measuring the capacitance and dielectric loss of the pellets sintered at different temperatures. The dielectric constants of the samples were calculated according to eq 2[29]

$$\kappa = C \cdot d \cdot \varepsilon_0^{-1} \cdot A^{-1} \tag{2}$$

κ is the dielectric constant, C is the measured capacitance, d is the thickness of the pellet, ε_0 is the electrical permittivity of vacuum space equal to $8.85 \cdot 10^{-12}$ m^{-3} kg^{-1} s^4 A^2, and A is the active surface of the electrodes. Figure 3a indicates the dielectric constants of the samples as a function of electrical field frequency in the range of 0.1−100 kHz. In all samples, the dielectric constant rapidly decreases with increasing frequency up to around 10 kHz and then continuously decreases at a reduced rate. At frequencies lower than a critical range (approx. 1 to 10 kHz, depending on the materials and measurement conditions), the dominant polarization contribution is assumed to result from the space-charge mechanism which, in **1**, sharply vanishes at frequencies around 1 kHz.[29] The dielectric constant of **1**-923 is around 1850 at a frequency of 1 kHz, significantly higher than some benchmark dielectric

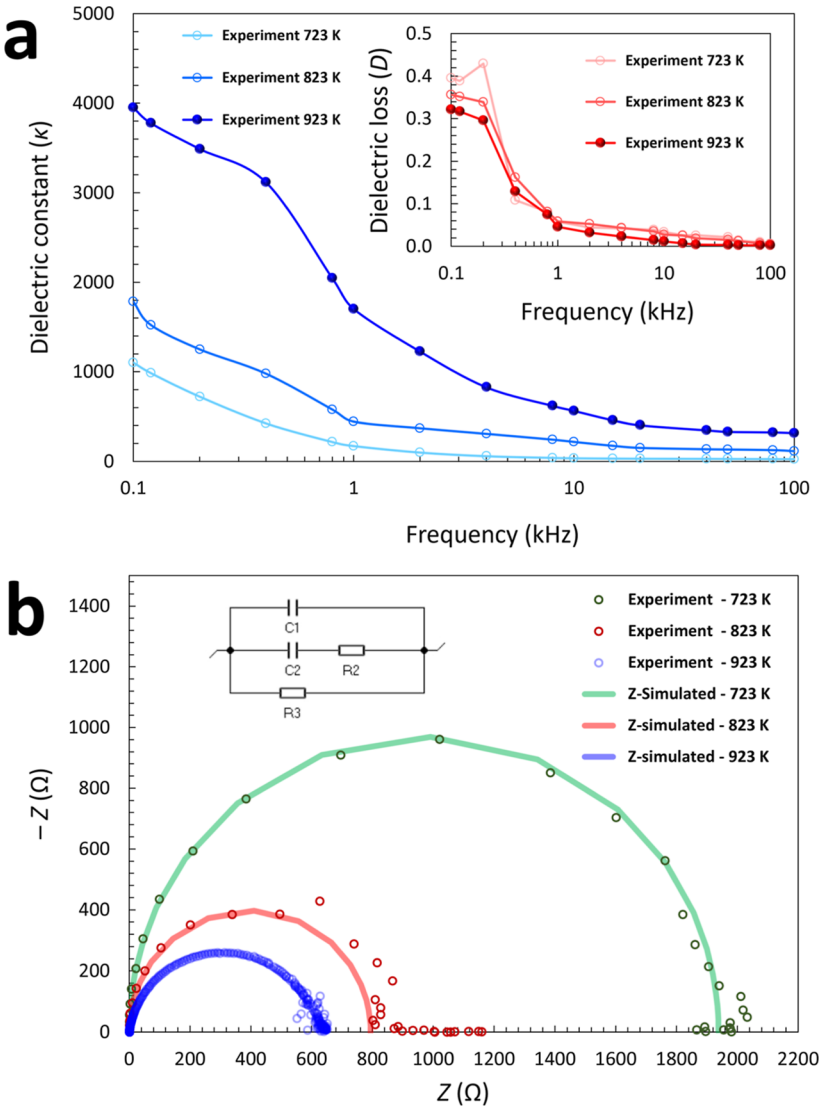

Figure 3. (a) Plot of the dielectric constant of **1** as a function of the frequency for pellets of **1**-723, **1**-823, and **1**-923. Inset: Plot of the dielectric loss of **1** as a function of the frequency. (b) Complex impedance plot of **1**, sintered at different temperatures, and the simulated curves according to an equivalent circuit (inset) including parallel series of capacitance (C) and resistance (R) sets according to the one arc model, while R3 is a resistor element for the electronic conductivity contribution.

materials such as barium and strontium titanates.[30] The dielectric constant of **1** is relatively high despite the dark color of the powder which corresponds to a comparably narrow band gap. The high dielectric constant might be explained by considering the inverse relationship of the dielectric constant with the band gap energy in semiconductors.[31,32] Additionally, the structural defects could play a role as an internal barrier layer capacitance (BLC) area. BLC is a well-known effect of enhancing the dielectric characteristics of capacitor materials.[31,32] Synergical impacts of these effects could lead to introduce a class of dielectric materials with narrower band gap energies.[31] At frequencies lower than 1 kHz, the measurements could be affected by the environmental noises such as thermal and electromagnetic noises, which can cause deviations from the ideal trends. Lower sintering temperatures result in lower dielectric constants. Samples of **1**-823 and **1**-723 indicate dielectric constants of 1002 and 998 at 1 kHz, respectively. The dependency of dielectric constants to the sintering temperature can be explained by the considerable impacts of the sintering temperature on the grain-to-grain boundary ratio and bulk density of materials as a well-known phenomenon in electronic materials.[33] At higher temperatures, a higher number of sintering mechanisms are activated, leading to potentially higher bulk density of materials.[34] Lower sintering temperatures result in lower dielectric constants.[35] In addition, the higher sintering temperature could facilitate the grain growth and lead to an increase in the grain-to-grain-boundary ratio. The FE-SEM micrographs of the microstructure of the pellets sintered at different temperatures are provided in the Supporting Information, Figure S2, indicating the larger average size of grains for the samples sintered at higher temperatures.

In a similar trend, the dielectric losses of all samples are decreased for an increase of the measurement frequency, while the sample sintered at higher temperature shows lower loss values (Figure 3a, inset frame). The dielectric losses of **1**-923, **1**-823, and **1**-723 are around 0.045, 0.057, and 0.059, respectively, at 1 kHz. The electrical resistivity and conductivity of the samples were measured and are provided in the Supporting Information, indicating a decrease of

resistivity from around 140 Ω·cm at 100 Hz to around 65 Ω·cm at 100 kHz as well as an increase of conductivity from around 6.5 mS·cm^{-1} at 100 Hz to around 15.8 mS·cm^{-1} at 100 kHz.

Complex impedance measurements at ambient temperature were carried out to investigate the transport properties of the samples by plotting the Nyquist curves of real and imaginary parts of the impedance. Figure 3b displays the complex impedance plots of samples sintered at different temperatures in the frequency range of 100 mHz to 1 MHz. Plots for all samples indicate a single semicircular trend, indicating an electrical conductivity with electronic leakage.[36] In most of the alkali metal-ion superconductors, the semicircular Nyquist curves indicate an obvious linear tail in the post-region of intersections with the real impedance (Z) as one of the characteristics of ionic superconductivity of materials.[4,10] However, in Figure 3b, there is no significant linear part after the intersection points, indicating a contribution of the electronic conductivity. Simulations were carried out by designing different equivalent circuits including and excluding an electronic contribution, as well as grain−grain boundary models (see Supporting Information).[34,36] In **1**-923, simulations with equivalent circuits including an additional resistor for an electronic contribution and based on the one arc model resulted in curves with considerably higher congruency compared to the circuits designed based on the grain−grain boundary model or without an electronic conductivity contribution and were thus applied for all samples. The intersections of the curves with the Z axis were considered as the total bulk resistivity of the samples to approximate their ionic conductivity. The value of the bulk resistivity is decreased by increasing the sintering temperature, from approx. 1946 Ω for the sample of **1**-723, to 809 Ω for **1**-823, and to 628 Ω for **1**-923. As the sintering at higher temperature principally results in a higher density of the bulk material,[33,34] the potential porosities within the samples sintered at lower temperatures can act as nonconductive barriers for the ion transfer through the microstructure. The experimentally determined band gap of 1.64 eV (vide infra), in combination with Fe−Fe distances of 2.6808(4)−3.8495(3) Å, would not suggest a predominant electronic contribution to the electrical impedance, while a predominant ionic Na···S interaction, the high dielectric values that sharply drop at comparably low frequencies, and the presence of statistically distributed Fe vacancies would suggest an ionic contribution. However, the absence of a post-intersect tail, as well as a potential redox activity of the iron ions, renders the calculated ionic conductivity of 3.42 mS·cm^{-1} with an activation energy of 0.324 eV (based on the equivalent circuit as depicted in Figure 3) for **1**-923 only a rough approximation. To comprehensively study the different contributions to the electrical conductivity, the design of an electrochemical cell comprising **1**, as well as further experimental studies, is planned.

3.2.1. Magnetic Properties. Field-dependent magnetization curves of **1** under the application of an external magnetic field up to 5.00 T at different temperatures are plotted in Figure 4a. The increase of the measurement temperature from 3 to 100 K results in the decrease of the magnetization from around 8.12 to −4.36 Am^2·kg^{-1} under an external applied field of 5.00 T. For temperatures higher than 100 K, the magnetization values under the same field are sharply reduced to 0.42 at 200 K and 0.17 at 300 K. At all temperatures, the curves' trend is linear, particularly at temperatures higher than 100 K. As a possible

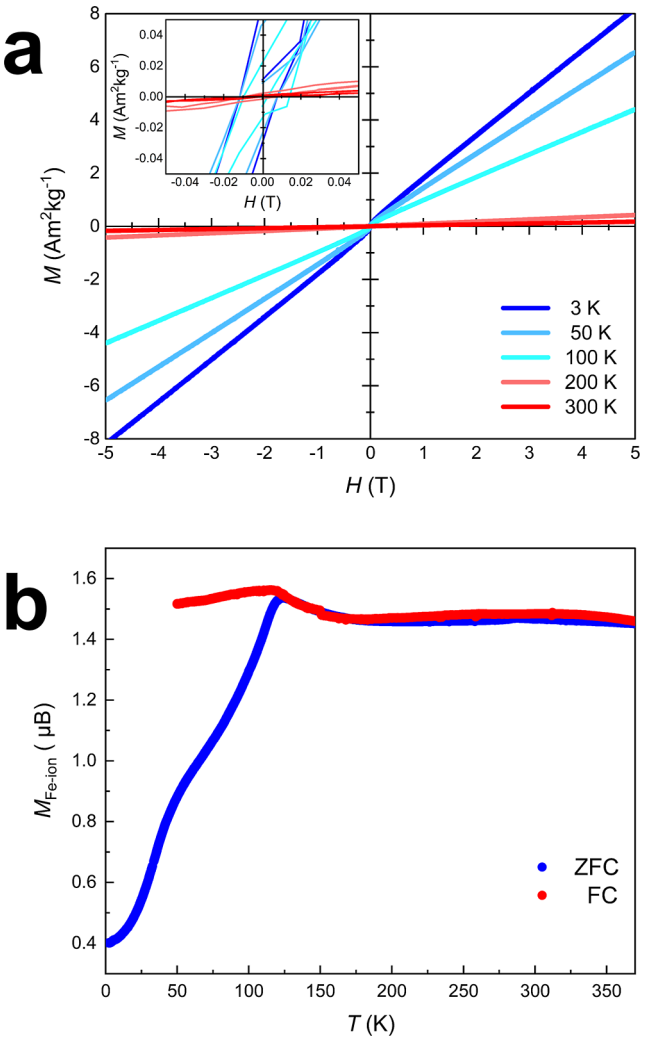

Figure 4. (a) Field-dependent magnetization curves for **1** at different temperatures as a function of the external applied field up to 5.00 T. (b) ZFC and FC plots of **1** as a function of measurement temperature under an applied field of 50 mT.

explanation for the observed hysteresis cycles in the field-dependent magnetization plots at temperatures lower than 100 K, the potential existence of spin canting in the antiferromagnetic order could act as a localized disordered area with deviation from the ideal antiferromagnetic structure and induce the coercivity and remanence in the hysteresis loops. This possibility can be supported by an initial saturation plateau at low fields and then a linear increase with increasing DC field strength. Figure 5b depicts the results of temperature-scan measurements including FC and ZFC curves in the temperature range of 3−370 K under an applied field of 50 mT. An increase of the temperature enhances the magnetization in the ZFC curve up to 1.56 μB at around 120 K and is reduced at further increased temperatures. At the temperature of 120 K, there is a bump in the FC curve, which is matched with the bifurcation point of the FC and ZFC curves, which is considered a transition in the magnetic properties. At 50 mT field, the magnetization remains almost constant as a function of the temperature above 120 K with a moment of 1.48 μB. This is a strong hint toward ferromagnetism at higher temperature; however, field-dependent magnetization curves indicate no coercivity and remanence in this range of

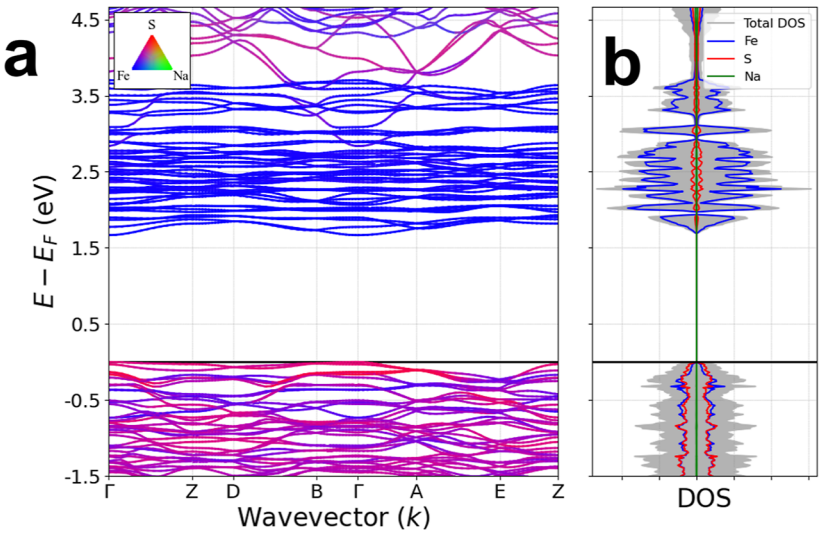

Figure 5. (a) Calculated elemental-resolved electronic band structure of **1**. (b) Calculated DOS of **1**, including total and elemental-resolved DOS plots.

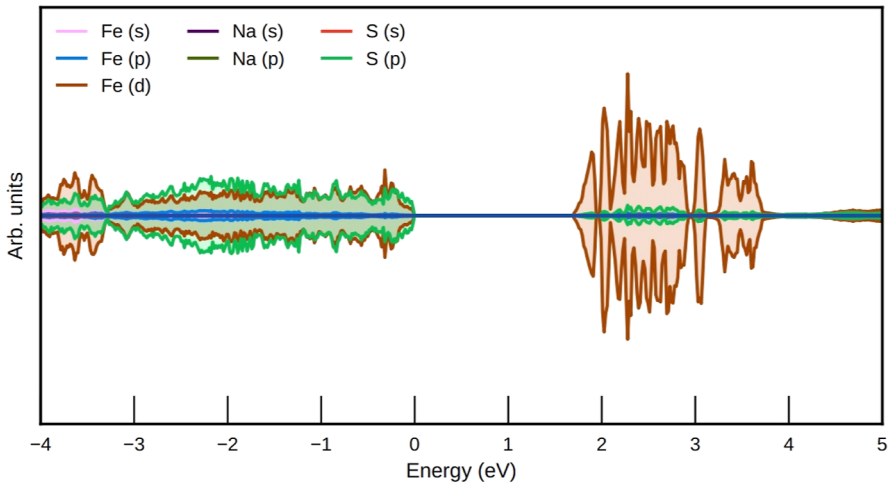

Figure 6. Spin-resolved DOS of **1** computed based on the DFT + U method.

temperature. The plot of the magnetic susceptibility times the temperature versus the temperature (χ·T − T), in the temperature range of 3−370 K, is provided in the Supporting Information, indicating a transition at a temperature of around 120 K. Due to the complex structure resulting from the statistical occupation of iron atoms, it is impossible to assign ferro- and antiferromagnetic ordering based on the X-ray crystallographic structure model. Future investigations such as neutron diffraction technique as well as elemental-specific methods, e.g., using X-ray absorption spectroscopy, would be beneficial to obtain a more accurate description of the magnetic structure and moments.

According to the trends of the curves in both field-dependent magnetization and temperature-scan plots, **1** is an antiferromagnetic compound with a Néel temperature of around 120 K. The sharp decrease of magnetization in Figure 4a could be related to a magnetic phase transition. The small hysteresis in the field-dependent magnetization curves at temperatures lower than 100 K could be related to additional intrinsic or extrinsic defects in the crystal structure.

3.3. UV−Visible Spectroscopy and Electronic Band Structure. Figures S6 and S7 display the Tauc plot of **1** for the direct and indirect transitions, respectively, derived from UV−visible measurements, indicating a direct optical band gap of around 1.64 eV. The electronic band structure and DOS of **1** were computed by DFT calculations. The computed element-resolved band structure (Figure 5a) demonstrates a direct band gap of 1.673 eV, obtained with the GGA + U method, when different U_{eff} values lead to variation in the computed band gaps (Figure S8).

The valence band maximum and the conduction band minimum are located at the Γ-point. From the DOS in Figure 5b, a considerable hybridization between Fe and S orbitals populating the valence band near the Fermi level is observable. In Figure 6, the conduction bands are dominated by the Fe 3d states with partial hybridizations with S 3p states. The DOS is completely symmetrical due to the antiferromagnetic nature of **1** (see Figure S9).

We note in passing that GGA-PBE and its revised version for solids and surfaces (PBESol)[37] falsely predict **1** to be of metallic nature. With a strongly constrained and appropriately normed metageneralized gradient approximation (SCAN) functional, a narrow band gap of 0.257 eV was obtained

(Figure S10). The complementary details of the calculations and their results are provided in the Supporting Information.

4. CONCLUSIONS

$Na_2[Fe_3S_4]$ with a layered anionic sublattice and 25% statistical iron vacancies was synthesized by means of a straightforward and fast solid- state method based on the high-temperature treatment of precursors containing abundant elements. The compound depicts a trigonal crystal lattice with honeycomb-shaped cavities and cationic layers of sodium ions. Measurements of the dielectric and the complex electrochemical impedance properties display a high dielectric constant of up to 1850 at a frequency of 1 kHz as well as semicircular arc of complex impedance with the bulk electrical resistivity values in the range of 628 to 1946 Ω, indicating the tunability of these properties as a function of the sintering temperature. Further optical investigations indicate the semiconductivity of **1** with a direct band gap of 1.64 eV. Magnetometry results illustrate an antiferromagnetic structure with a Néel temperature of 120 K. Therefore, **1** is a multifunctional material with a sustainable elemental combination and potential for application in electronic and magnetic applications.

Accession Codes

CCDC 2232589 contains the supplementary crystallographic data for this paper. These data can be obtained free of charge via www.ccdc.cam.ac.uk/data_request/cif, or by emailing data_request@ccdc.cam.ac.uk, or by contacting The Cambridge Crystallographic Data Centre, 12 Union Road, Cambridge CB2 1EZ, UK; fax: +44 1223 336033.

AUTHOR INFORMATION

Corresponding Author

Günther Thiele − *Fachbereich Biologie, Chemie, Pharmazie, Freie Universität Berlin, Berlin 14195, Germany;* orcid.org/0000-0003-2935-9335; Phone: +49 30 838 64881; Email: guenther.thiele@fu-berlin.de

Authors

Mohammad R. Ghazanfari − *Fachbereich Biologie, Chemie, Pharmazie, Freie Universität Berlin, Berlin 14195, Germany*

Konrad Siemensmeyer − *Helmholtz-Zentrum Berlin für Materialien und Energie, Berlin 14109, Germany*

Archa Santhosh − *Institute of Hydrogen Technology, Helmholtz-Zentrum Hereon, Geesthacht 21502, Germany*

Johannes C. Vrijmoed − *Fachbereich Geowissenschaften, Freie Universität Berlin, Berlin 12249, Germany*

Mirko Tallu − *Institute of Nanotechnology (INT), Karlsruhe Institute of Technology (KIT), Eggenstein-Leopoldshafen 76344, Germany*

Stefanie Dehnen − *Institute of Nanotechnology (INT), Karlsruhe Institute of Technology (KIT), Eggenstein-Leopoldshafen 76344, Germany;* orcid.org/0000-0002-1325-9228

Paul Jerabek − *Institute of Hydrogen Technology, Helmholtz-Zentrum Hereon, Geesthacht 21502, Germany;* orcid.org/0000-0002-2995-9755

Author Contributions

Conceptualization: M.R.G., G.T.; project administration: M.R.G., G.T., writing initial draft: M.R.G.; formal analysis: M.R.G.; investigation of magnetic properties: K.S.; performance and visualization of DFT calculations: A.S.; investigation via EDX and SEM: J.C.V.; investigation of UV−visible spectroscopy measurements: M.T.; resources for UV−visible spectroscopy measurements: S.D.; resources for DFT calculations: P.J.; resources for synthesis, impedance and dielectric properties: G.T.; funding acquisition: G.T.; review and editing: G.T.; supervision: G.T., P.J. All authors have given approval to the final version of the manuscript.

Notes

The authors declare no competing financial interest.

ACKNOWLEDGMENTS

We thank the Verband der Chemischen Industrie e.V. for a Liebig scholarship, the Volkswagen Stiftung within the framework of an "Experiment!" funding, the German-American Fulbright Commission for a Fulbright- Cottrell Award. The authors acknowledge the North-German Supercomputing Alliance (HLRN) for providing High-Performance Computing (HPC) resources that have contributed to the research results. Core facility BioSupraMol is acknowledged for X-ray diffraction time. We thank Prof. Nicola Pinna and Dr. Patricia Russo for the PXRD measurement time at Humboldt Universität zu Berlin. We thank Friederike Fuß, Asad Malik, Ayla Karnas, and Jan-Erik Fuhrmann for their support in UV−visible spectroscopy, PXRD, and TG/DSC measurements. We thank Dr. Karel Prokes and the Quantum Materials Core Lab facilities at Helmholtz-Zentrum Berlin (HZB) for the magnetic measurements.

REFERENCES

(1) Jiang, Y.; Tian, B. Inorganic Semiconductor Biointerfaces. *Nat. Rev. Mater.* **2018**, *3*, 473−490.

(2) Qi, L.; Petersson, L.; Liu, T. Review of Recent Activities on Dielectric Films for Capacitor Applications. *J. Int. Counc. Electr. Eng.* **2014**, *4*, 1−6.

(3) Zhang, X.; Yang, G. Recent Advances and Applications of Inorganic Electrides. *J. Phys. Chem. Lett.* **2020**, *11*, 3841−3852.

(4) Xie, D.; Zhang, M.; Wu, Y.; Xiang, L.; Tang, Y. A Flexible Dual-Ion Battery Based on Sodium-Ion Quasi-Solid-State Electrolyte with Long Cycling Life. *Adv. Funct. Mater.* **2020**, *30*, 1906770.

(5) Wang, Y.; Chen, R.; Chen, T.; Lv, H.; Zhu, G.; Ma, L.; Wang, C.; Jin, Z.; Liu, J. Emerging non-lithium Ion Batteries. *Energy Storage Mater.* **2016**, *4*, 103−129.

(6) Sharma, S. S.; Manthiram, A. Towards More Environmentally and Socially Responsible Batteries. *Energy Environ. Sci.* **2020**, *13*, 4087−4097.

(7) Huang, H.; Xu, R.; Feng, Y.; Zeng, S.; Jiang, Y.; Wang, H.; Luo, W.; Yu, Y. Sodium/Potassium-Ion Batteries: Boosting the Rate Capability and Cycle Life by Combining Morphology, Defect and Structure Engineering. *Adv. Mater.* **2020**, *32*, 1904320.

(8) Wu, X.; Markir, A.; Xu, Y.; Hu, E. C.; Dai, K. T.; Zhang, C.; Shin, W.; Leonard, D. P.; Kim, K.; Ji, X. Rechargeable Iron−Sulfur

Battery without Polysulfide Shuttling. *Adv. Energy Mater.* **2019**, *9*, 1902422.
(9) Chen, X.; Zhou, Z.; Karahan, H. E.; Shao, Q.; Wei, L.; Chen, Y. Recent Advances in Materials and Design of Electrochemically Rechargeable Zinc−Air Batteries. *Small* **2018**, *14*, 1801929.
(10) Leube, B. T.; Salager, E.; Chesneau, E.; Rousse, G.; Vezin, H.; Abakumov, A. M.; Tarascon, J. M. Layered Sodium Titanium Trichalcogenide Na_2TiCh_3 Framework (Ch = S, Se): A Rich Crystal and Electrochemical Chemistry. *Chem. Mater.* **2022**, *34*, 2382−2392.
(11) Ghazanfari, M. R.; Santhosh, A.; Siemensmeyer, K.; Fuß, F.; Staab, L.; Vrijmoed, J. C.; Peters, B.; Liesegang, M.; Dehnen, S.; Oeckler, O.; Jerabek, P.; Thiele, G. Large Exchange Bias, High Dielectric Constant, and Outstanding Ionic Conductivity in a Single-Phase Spin Glass. *Adv. Electron. Mater.* **2022**, *8*, 2200483.
(12) Oei, D.-G. Sodium-sulfur system. II. Polysulfides of sodium. *Inorg. Chem.* **1973**, *12*, 438−441.
(13) (a) Rietveld, H. M. Line Profiles of Neutron Powder-diffraction Peaks for Structure Refinement. *Acta. Cryst.* **1967**, *22*, 151−152. (b) Rietveld, H. M. A Profile Refinement Method for Nuclear and Magnetic Structures. *J. Appl. Crystallogr.* **1969**, *2*, 65−71.
(14) Toby, B. H.; von Dreele, R. B. GSAS-II: The Genesis of a Modern Open-source All Purpose Crystallography Software Package. *J. Appl. Crystallogr.* **2013**, *46*, 544−549.
(15) Fuß, F.; Rieckert, M.; Steinhauer, S.; Liesegang, M.; Thiele, G. 3D-printed Equipment to Decouple (P)XRD Sample Preparation and Measurement. *J. Appl. Cryst.* **2022**, *55*, 686−692.
(16) Dolomanov, O. V.; Bourhis, L. J.; Gildea, R. J.; Howard, J. A. K.; Puschmann, H. OLEX2: A Complete Structure Solution, Refinement and Analysis Program. *J. Appl. Crystallogr.* **2009**, *42*, 339−341.
(17) Sheldrick, G. M. SHELXT - Integrated Space-group and Crystal-structure Determination. *Acta Crystallogr. A* **2015**, *71*, 3−8.
(18) Sheldrick, G. M. Crystal Structure Refinement with SHELXL. *Acta Crystallogr. C* **2015**, *71*, 3−8.
(19) Brandenburg, K.. *DIAMOND 4*; Crystal Impact GbR: Bonn, 2020; Vol. *6.4*.
(20) Osman, Z.; Mohd Ghazali, M. I.; Othman, L.; Md Isa, K. B. AC Ionic Conductivity and DC Polarization Method of Lithium-ion Transport in PMMA−$LiBF_4$ Gel Polymer Electrolytes. *Results Phys.* **2012**, *2*, 1−4.
(21) *AMETEK Princeton Applied Research DataBase*, 2022 Electrochemical Software, https://www.ameteksi.com/library/application-notes/princeton-applied-research. Accessed 27 October 2022.
(22) Kokhanovsky, A. A. Physical Interpretation and Accuracy of the Kubelka−Munk Theory. *J. Phys. D: Appl. Phys.* **2007**, *40*, 2210−2216.
(23) Kresse, G.; Furthmüller, J. Efficient Iterative Schemes for Ab Initio Total-energy Calculations using a Plane-wave Basis Set. *Phys. Rev. B* **1996**, *54*, 11169−11186.
(24) Perdew, J. P.; Burke, K.; Ernzerhof, M. Generalized Gradient Approximation Made Simple. *Phys. Rev. Lett.* **1996**, *77*, 3865−3868.
(25) Hammer, B.; Hansen, L. B.; Norskov, J. K. Improved adsorption energetics within density-functional theory using revised Perdew-Burke-Ernzerhof functionals. *Phys. Rev. B* **1999**, *59*, 7413−7421.
(26) Lai, X.; Chen, X.; Jin, S.; Wang, G.; Zhou, T.; Ying, T.; Zhang, H.; Shen, S.; Wang, W. New Layered Iron Sulfide $NaFe_{1.6}S_2$: Synthesis and Characterization. *Inorg. Chem.* **2013**, *52*, 12860−12862.
(27) Stüble, P.; Peschke, S.; Johrendt, D.; Röhr, C. $Na_7[Fe_2S_6]$, $Na_2[FeS_2]$ and $Na_2[FeSe_2]$: New ‚Reduced' Sodium Chalcogenido Ferrates. *J. Solid State Chem.* **2018**, *258*, 416−430.
(28) Bronger, W.; Balk-Hardtdegen, H.; Ruschewitz, U. Darstellung Struktur und Magnetische Eigenschaften der Natriummeisenchalkogenide Na_6FeS_4 und Na_6FeSe_4. *Z. Anorg. Allg. Chem.* **1992**, *616*, 14−18.
(29) Bao, W.; Li, G. N.; Huang, Q. Z.; Chen, G. F.; He, J. B.; Wang, D. M.; Green, M. A.; Qiu, Y. M.; Luo, J. L.; Wu, M. M. Superconductivity Tuned by the Iron Vacancy Order in $K_xFe_{2-y}Se_2$. *Chin. Phys. Lett.* **2013**, *30*, 027402.
(30) Bain, A. K.; Chand, P.; *Ferroelectrics: Principles and Applications*. st Edition, 1; Wiley-VCH Verlag GmbH, 2017, pp 6−22.
(31) Wu, L.; Zhu, Y.; Park, S.; Shapiro, S.; Shirane, G.; Tafto, J. Defect Structure of the High-Dielectric-Constant Perovskite $CaCu_3Ti_4O_{12}$. *Phys. Rev. B* **2005**, *71*, 014118.
(32) Liu, D.; Tse, K.; Robertson, J. Electronic Structure and Defects of High Dielectric Constant Gate Oxide $La_2Hf_2O_7$. *Appl. Phys. Lett.* **2007**, *90*, 062901.
(33) Ardakani, H. A.; Alizadeh, M.; Amini, R.; Ghazanfari, M. R. Dielectric Properties of $CaCu_3Ti_4O_{12}$ Improved by Chromium/Lanthanum Co-doping. *Ceram. Int.* **2012**, *38*, 4217−4220.
(34) Riquet, G.; Marinel, S.; Bréard, Y.; Harnois, C. Sintering Mechanism and Grain Growth in $CaCu_3Ti_4O_{12}$ Ceramics. *Ceram. Int.* **2019**, *45*, 9185−9191.
(35) Mishra, P.; Sonia; Kumar, P. Effect of Sintering Temperature on Dielectric, Piezoelectric and Ferroelectric Properties of BZT−BCT 50/50 Ceramics. *J. Alloys Compd.* **2012**, *545*, 210−215.
(36) Huggins, R. A. Simple Method to Determine Electronic and Ionic Components of the Conductivity in Mixed Conductors A Review. *Ionics* **2002**, *8*, 300−313.
(37) Perdew, J. P.; Ruzsinszky, A.; Csonka, G. I.; Vydrov, O. A.; Scuseria, G. E.; Constantin, L. A.; Zhou, X.; Burke, K. Restoring the Density-Gradient Expansion for Exchange in Solids and Surfaces. *Phys. Rev. Lett.* **2008**, *100*, 136406.